Bull. Min. Res. Exp. (2024) 173: 235-252

Bulletin of the Mineral
Research and Exploration

http://bulletin.mta.gov.tr

Anthropogenic problems threatening major cities: Largest surface deformations observed in Hatay, Türkiye based on SBAS-InSAR

Şükrü Onur KARACA[a*], Gültekin ERTEN[a], Semih ERGİNTAV[b] and Shuhab D. KHAN[c]

[a] *General Directorate of Mineral Research and Exploration, Department of Geological Research, Remote Sensing and GIS Division, Ankara, Türkiye*
[b] *Boğaziçi University, Kandilli Observatory and Earthquake Research Institute, Department of Geodesy, İstanbul, Türkiye*
[c] *University of Houston, Department of Earth and Atmospheric Sciences, Houston, TX, USA*

Research Article

Keywords:
Multi-temporal InSAR,
Radar interferometry,
Surface deformation,
Hatay-Güzelburç,
Türkiye.

ABSTRACT

The surface deformation caused by tectonic activities and anthropogenic factors poses a great threat to cities worldwide. The investigation and monitoring of these deformations are crucial in order to create risk analysis for the future. The problem in this case is to investigate the surface deformations and their negative effects caused by groundwater use and to identify possible landslide areas. In this study, the surface deformations in Hatay province were analyzed using SBAS-InSAR. The results from these analyses were evaluated by field observations. Sentinel-1 descending (183 datasets) and ascending (147 datasets) track geometries were selected to determine the surface deformation and its temporal evolution. Both east-west and vertical surface deformations were calculated, and the surface deformation profiles, surface 3D models and time series were created. These time series were associated with monthly precipitation data. The deformation area was interpreted with regard to available well-log data and geological setting of the study area. As a result of the study, a surface deformation resembling a bowl like structure was observed in the industrial zone located in the city center of Hatay-Güzelburç. The deformation rates are approximately 22.3 cm/year in the form of subsidence, 3.6 cm/year in the form of eastern movement and 10.1 cm/year in the form of western movement. The deformation of this bowl-like structure decelerated in the winter and accelerated in the summer due to excessive water use. The average monthly precipitation dataset supports these results. The stratigraphic data from water wells and the presence of limestone outside the eastern boundary of the deformation area show a thick clay layer in the eastern block of the bowl-shaped deformation structure. The difference between these two units, which causes a sharp anomaly at the eastern border of the deformation area, is interpreted as a probable normal fault. The second study area where surface deformations are observed is the landslide zone. The deformation was found to be 7.5 cm/year in a westward direction and 1.5 cm/year as subsidence.

Received Date: 08.02.2023
Accepted Date: 17.05.2023

1. Introduction

The surface deformation induced by geological processes causes widespread infrastructural damage in urban areas and is a common geological hazard worldwide. Numerous studies have been conducted by researchers to detect and understand landform deformations using satellite systems and radar interferometry (Amelung et al., 1999; Strozzi et al., 2001; Raucoules et al., 2007; Zhang et al., 2012; Khan et al., 2014; Motagh et al., 2017; Solari et al., 2018). Interferometric Synthetic Aperture Radar (InSAR) is one of the methods widely used in recent years to investigate surface deformations. This method utilizes

---

Citation Info: Karaca, O., Ş., Erten G., Ergintav S. Khan D. S., 2024. Anthropogenic problems threatening major cities: Largest surface deformations observed in Hatay, Türkiye based on SBAS-InSAR. Bulletin of the Mineral Research and Exploration 173, 235-252. https://doi.org/10.19111/bulletinofmre.1298494

Corresponding author: Şükrü Onur KARACA, onurkaraca87@ hotmail.com

the phase difference between the radar image pairs to determine the deformation rates of various surface motions (Hung et al., 2011; Tomás et al., 2014; Brunori et al., 2015; Aslan et al., 2018; Khan et al., 2022).

One of the most common factors that cause subsidence in major cities is the excessive use of groundwater (Motagh et al., 2007; Anderssohn et al., 2008; Tomás and Li, 2017). For example, one of the highest subsidence rates of 3,5 cm/year is reported from Mexico City that is caused by the excess pumping of groundwater (Strozzi and Wegmuller, 1999; Cabral-Cano et al., 2008; Lopez-Quiroz et al., 2009; Osmanoğlu et al., 2011; Yan et al., 2012; Cabral-Cano et al., 2015; Sowter et al., 2016; Cigna and Tapete, 2021). Another area that shows extensive land subsidence is in the vicinity of Konya, Türkiye. Konya City is located in the Central Türkiye that displays karstic terrain of highly erodible rocks typical of the Mediterranean and the Central Anatolia regions of Türkiye. Since karstic units in such regions have a structure that is easily soluble in water especially when groundwater combines with carbon dioxide, they form large cavities in underground called sinkholes (Ford and Williams, 1989; Waltham and Fookes, 2003). One of the study conducted by Orhan (2021) in the Karapınar district of Konya revealed that there was 7 cm/year of subsidence in this area using InSAR, Global Navigation Satellite System (GNSS) and groundwater level data. Another study conducted in Konya province determined the amount of subsidence in the region between the years 2004 and 2020 using Envisat, ALOS-1, and modeled this subsidence area by Sentinel-1 A/B data (Şireci et al., 2021). İmamoğlu et al. (2019) carried out a study in the Turkish province of Afyon - Bolvadin region which has similar geology and structure to Konya. İmamoğlu et al. (2019) utilized InSAR to analyze the surface deformations (Sentinel-1 dataset between 2014-2018) and compared the results with the geology of the region, groundwater data and field observations in his study. Maximum subsidence of 3.5 cm/year observed in the southern part of the study area shows that this area is characterized by the presence of soft alluvial deposits. They stated that the northeastern part of the deformed region composed of slope debris and pebbles has a relatively lower subsidence rate (İmamoğlu et al., 2019). Aslan et al. (2019) characterized and monitored the subsidence of the Bursa Plain (the southern Marmara region of Türkiye). They measured the subsidence patterns and correlated them with the lithology by using InSAR data and suggested a strong lithological control on subsidence. They concluded that the maximum rate of ground subsidence occurs where agricultural activity relies on groundwater exploitation (Aslan et al., 2019).

According to the “Geological and Geophysical Preliminary Survey Report for Hatay - Güzelburç Municipality Settlement Area (Türkiye)” prepared by the General Directorate of Natural Disasters in 2006, a remarkable deformation of the ground in the settlements, serious cracks in houses and buildings of the area were investigated. It was reported that the deformations in the region increased especially in 2004-2005, therefore some houses were completely evacuated or demolished (Kuran et al., 2006).

This study aims to reveal the surface deformations, boundaries, and causes of surface deformations around Hatay province, including the Güzelburç neighborhood with InSAR-SBAS, and to evaluate the results with field studies, average precipitation data, and geology of the region. This study is an attempt to reveal the surface deformations and their causes in Hatay province and to analyze the risks that may occur in the future due to surface deformation. In this context, this study presents suggestions for the effects of identified deformation on populated areas, determines their boundaries, investigates the risks arising from deformation, and reveals the causes and solutions to the problems related to the deformation for industrial zone.

As a cost-effective monitoring method, InSAR-SBAS technology has been considerably practiced in landslide identification and deformation monitoring. (Yao et al., 2017, 2022; Liu at al., 2021). We also try to identify landslide zone comprehensively and determine deformation characteristics.

2. Tectonic and Geological Setting of the Study Area

The Hatay Triple Junction (HTJ), defined as a tectonically complex region in southeastern Türkiye and northwestern Syria that forms the plate boundary between Arabia, Africa, and Anatolia, is located at the intersection of the left-lateral thrust East Anatolian Fault (EAF), west of the Cyprus Plunge Arc (CA) and north of the Dead Sea Fault (DSF) (Figure 1a) (Mahmoud et al., 2005, 2013). The study area covers the city center of Hatay province focusing on surface deformation in two different regions (Figure 1b). The first region is the industrial zone, which spans the area where the Asi River meanders relatively north of the study area (Figure 1c); and the second region is the landslide zone in the south of the study area (Figure 1d).

The geology of the region was well described in Sarıfakıoğlu's (2018) study, and the well-log data obtained from the General Directorate of State Hydraulic Works (DSI) was used. The bedrock of the region consists of the Kızıldağ Ophiolite (Kko) of the Cenomanian-Turonian age. It is unconformably overlain by the Lutetian-Bartonian Okçular formation (Teo) and by discordantly overlain Aquitanian-Burdigalian Balyatağı Formation (Tmb) (consisting of conglomerates and sandstones). The Balyatağı Formation is discordantly overlain by the Sofular Formation (Tms) consisting of reefal limestones of the same age. The Tepehan Formation (Tmt) was deposited in the Langhian-Serravalian interval, and the Nurzeytin Formation (Tmn) was deposited in the Middle-Upper Miocene and consists of sandstone, clayey limestone, claystone and marl. The Samandağ Formation (Tpls) was discordantly deposited in the Pliocene and overlain by Quaternary alluvium (Qal) and Slope debris (Qym) (Figure 1e). The log

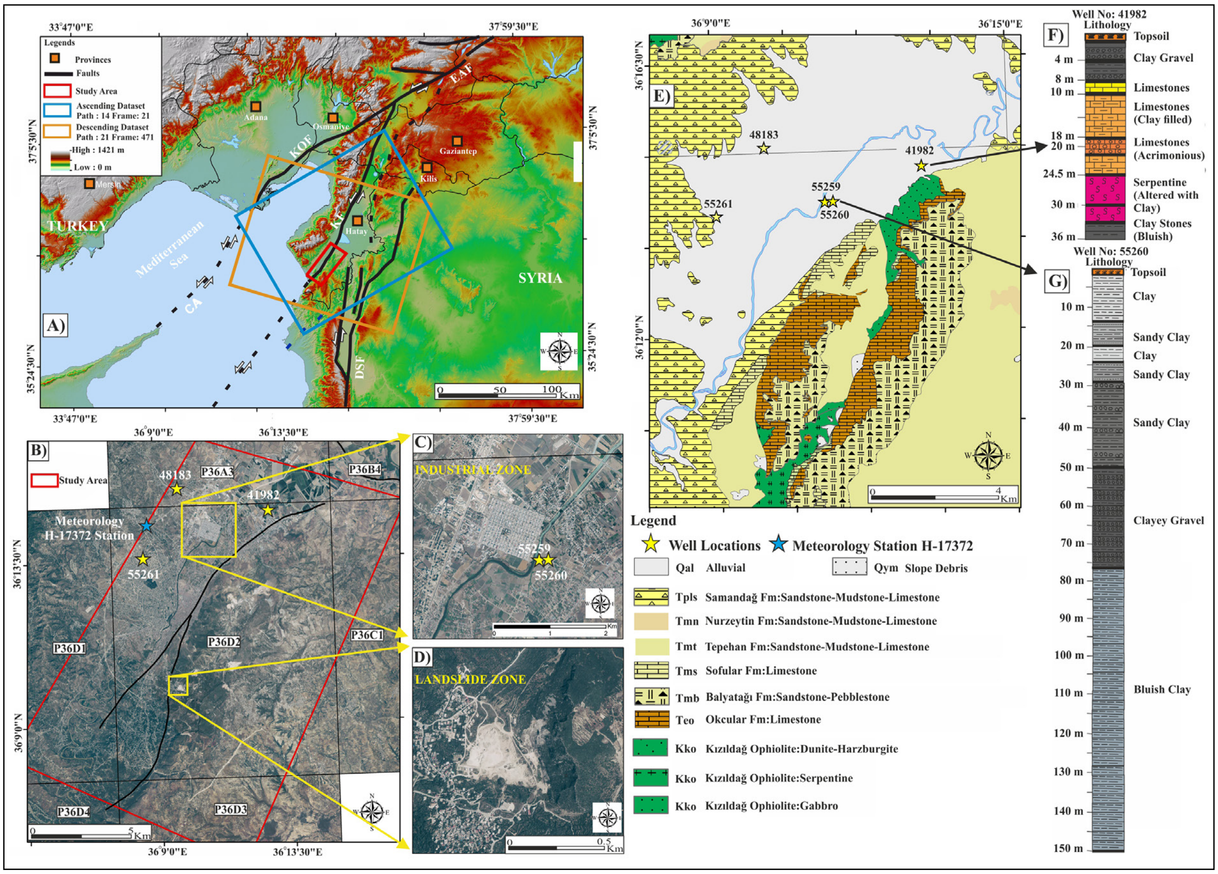

Figure 1- a) Digital elevation model (Aster-GDEM, 1 arc-sec - V2) of the study area. Red frame in the province of Hatay shows the study area. Ascending (path: 14, frame 114) and descending (path: 21, frame 471) geometry orthophoto datasets are represented with light blue and orange frames, respectively. Provinces in Türkiye are presented in orange squares. Abbreviations for faults: Dead Sea Fault, DSF; East Anatolian Fault, EAF; Karasu Fault, KF; Karataş-Osmaniye Fault, KOF; and Cyprus Arc, CA. Faults are modified after Mahmouda et al., (2013), b) The location map of the study areas. Yellow stars display the location of the wells, c) Industrial zone, d) Landslide zone (Orthophotos were obtained from the General Directorate of Mapping, 2022), e) Geological map (Sarıfakıoğlu, 2018), f) and g) well logs (Well data were obtained from the General Directorate of State Hydraulic Works (DSI), 2022).

of the well-41982 located on the eastern border of the deformation area shows limestone penetration immediately after a few meters of cover in the area (Figure 1f). Limestone unit continues to deposit until it comes in contact with a serpentinite unit at 24.5 m depth. The thickness of the relatively resistant limestone unit is approximately at 15-20 m depth (Figure 1f). This well lithology includes a thin layer of reefal limestone of the Sofular Formation followed by clayey limestone of the Tepehan Formation and finally serpentinites of the Kızıldağ Ophiolite. In contrast, the well 55260 (shown in Figure 1g) was drilled in clayey units that is succeeded by a sandy clay unit for 150 meters.

3. Materials and Methods

3.1. InSAR Method

Synthetic Aperture Radar Interferometry (InSAR) is a remote sensing method that can reveal surface deformations with centimeter-level accuracy and has wide coverage (Zebker and Goldstein, 1986; Rucci et al., 2012; Simons et al., 2015; Aimaiti et al., 2017). This geodetic method uses two or more synthetic aperture radar images to produce maps of surface deformation or digital elevation using differences in the phase of the waves returning to the satellite (Massonnet and Feigl, 1998; Burgmann et al., 2000).

3.2. SBAS (Small BAseline Subset) Method

SBAS method, which is a multi-temporal InSAR technique using multiple radar images, instead of the two radar images before and after the deformation, is currently used in many studies. Among these studies, the investigations of deformations caused by excess groundwater exploitation (Bell et al., 2008; Motagh et al., 2017; İmamoğlu et al., 2019; Orhan, 2021; Şireci et al, 2021), landslide occurrences (Zhu et al., 2014; Béjar-Pizarro et al., 2016; Liu et al., 2018, Liu et al., 2021) and active tectonic movements (Wöppelmann et al., 2013; Conesa-García et al., 2016 Karaca et al., 2021) can be considered.

SBAS, which is an InSAR algorithm, was first developed by Berardino et al. (2002) for the temporal assessment of surface deformations. Generally, in cases where the phase coherence in the preferred SAR data date ranges is low, the coherence between the most appropriate binary images cannot be established and it is difficult to reveal or observe surface deformations on the earth's surface. Several parameters affect the analysis of image pairs like weather conditions, topography, trajectory, geometric orthogonal base lengths, and temporal differences. To eliminate or minimize such factors, the SBAS algorithm was developed using multi-temporal (multiple) images (Berardino et al., 2002). In this study, the minimum temporal baseline was chosen to be 120 days for the city center and the normal baseline was chosen to be 5% to improve the consistency of the stacked image pairs with the vertical baseline threshold (Figure 2). A 1 arc-sec Shuttle Radar Topography Mission Height (SRTM HGT) (30 m) digital elevation model was used to enhance the topographic correction. In addition, the reference ground control points (GCPs) were selected on high coherence pixels without phase jumps (coherence > 0,7) to remove the ramp and phase constant during re-smoothing and refinement, away from actively deforming areas and evenly distributed across the study area. Additionally, atmospheric components were subtracted date by date from displacement measurements. The atmospheric correction is performed by the following two filtering procedures; Atmosphere low and high pass. Finally, in the geocoding process, the reference digital elevation model was used to transit from radar geometry to ground geometry (Figure 2). As a result of data processing, the surface deformation rates and displacement time series were generated. All data were processed in Envi 5.6.1-Sarscape 5.6.0 software (Figure 2).

In this study, Sentinel-1 147 ascending and 183 descending InSAR datasets (Table 1) were processed. In addition, 1 arc-sec Shuttle Radar Topography Mission Height (SRTM HGT) (30 m) was used as a digital elevation model.

3.3. Average Precipitation and Well Information Data

To investigate the correlation between the deformation areas in the region and groundwater level and the effect of monthly precipitation on deformation, the average precipitation data were obtained from the H-17372 station located in the study area from the General Directorate of Meteorology (Figure 1b).

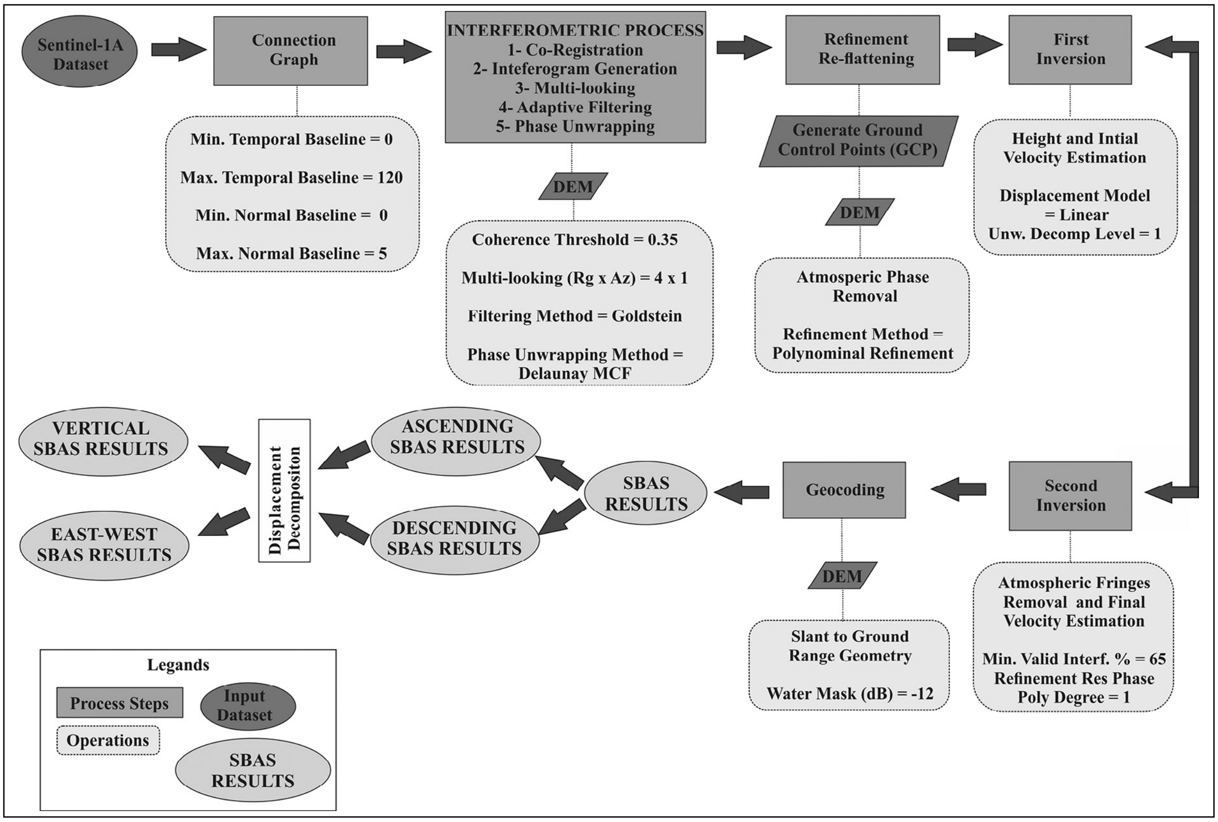

Figure 2- InSAR processing workflow using Small Baseline Subset technique.

Table 1- Information about Sentinel-1A/B datasets features. The product type is L1 single look complex (SLC) with ascending and descending geometry. Interferometric wide swath beam mode (IW). The following acronyms were used in the table: maximum perpendicular baseline (Bp) and maximum temporal baseline (Bt). Asc refers to ascending, des refers to descending. VH refers to cross-polarization which describes as vertical transmit and horizontal receive.

Product Type	Mode	Orbit Direction	Start Date	End Date	Quantity	Orbit	Path	Frame No.	Polarization	Wavelenght	Max Bp (%)	Max Bt (Days)
S1-A/B	IW	Ascending	2017/05/23	2022/02/26	147	18111	14	114	VH	5.6 cm	5	120
S1-A/B	**IW**	Descending	2015/11/19	2022/01/22	183	16893	21	471	VH	5.6 cm	5	120

However, any data, related to the static and dynamic information about the aquifer dynamics in the region is not available. Only, the station H-17372 were used due to availability and this monthly precipitation data cover same period of the InSAR dataset from 2015/11/19 to 2022/01/22. Additionally, this rainfall dataset was plotted with time series (Figure 4d and 4h).

4. Results and Discussion

4.1. Spatio-Temporal Properties of the Deformations

In this study, SAR images (ascending and descending) of Sentinel-1A satellite were used to determine the displacement rate of the center of Hatay province and its surrounding areas with the SBAS algorithm using the InSAR method. As it is known, one of the limitations of the InSAR method is that the results of the data processing give only the movement towards or away from the satellite direction. However, the ascending and descending images of the study area are applied together to estimate the east-west and upward-downward movements of the surface deformation. Accordingly, the InSAR-SBAS results for Hatay province were presented below.

The positions of the images used in data processing and image pairs for which interferograms were created are shown in Figures 3a and 3c, while Figures 3b and

3d show the base lengths between the image pairs for ascending and decreasing data sets, respectively. In Figure 3, the yellow diamonds represent the reference image pair (master) while the green diamonds represent the slave image pairs.

In Figure 4, descending and ascending Sentinel-1 datasets of Hatay province illustrate the results of SBAS analysis, respectively. In this figure, the negative values indicate the movement away from the satellite, while the positive values indicate the movement towards the satellite. In addition, in Figures 4D and 4H, the average monthly precipitation data and seasonal time information are shown together with the time series. To provide the vertical and horizontal velocity, the decomposition tool for descending and ascending geometries was applied. The ENVI SARscape tool decomposes the displacement and calculates local incidence angles. The two local incidence angles calculated are described as Inclination Line of Sight (ILOS) and Azimuth Line of Sight (ALOS). Consequently, the ascending and descending InSAR-SBAS results were evaluated together to obtain both east-west and up-down SBAS results (Figure 5). In Figures 4 and 5, all minimum and maximum velocities are shown in Table 2.

For industrial zone, figures 6a and 6b show the vertical and east - west surface deformation velocities. Figures 6c and 6d show interferograms, 6e and 6f show unwrapped phase, 6g and 6h show re-flattened unwrapped phase, and 6i and 6j show re-flattened filtered interferograms for both ascending and descending datasets. In Figure 6, all images depict a relatively more precise deformation difference on the west side of the industrial zone than on the east side

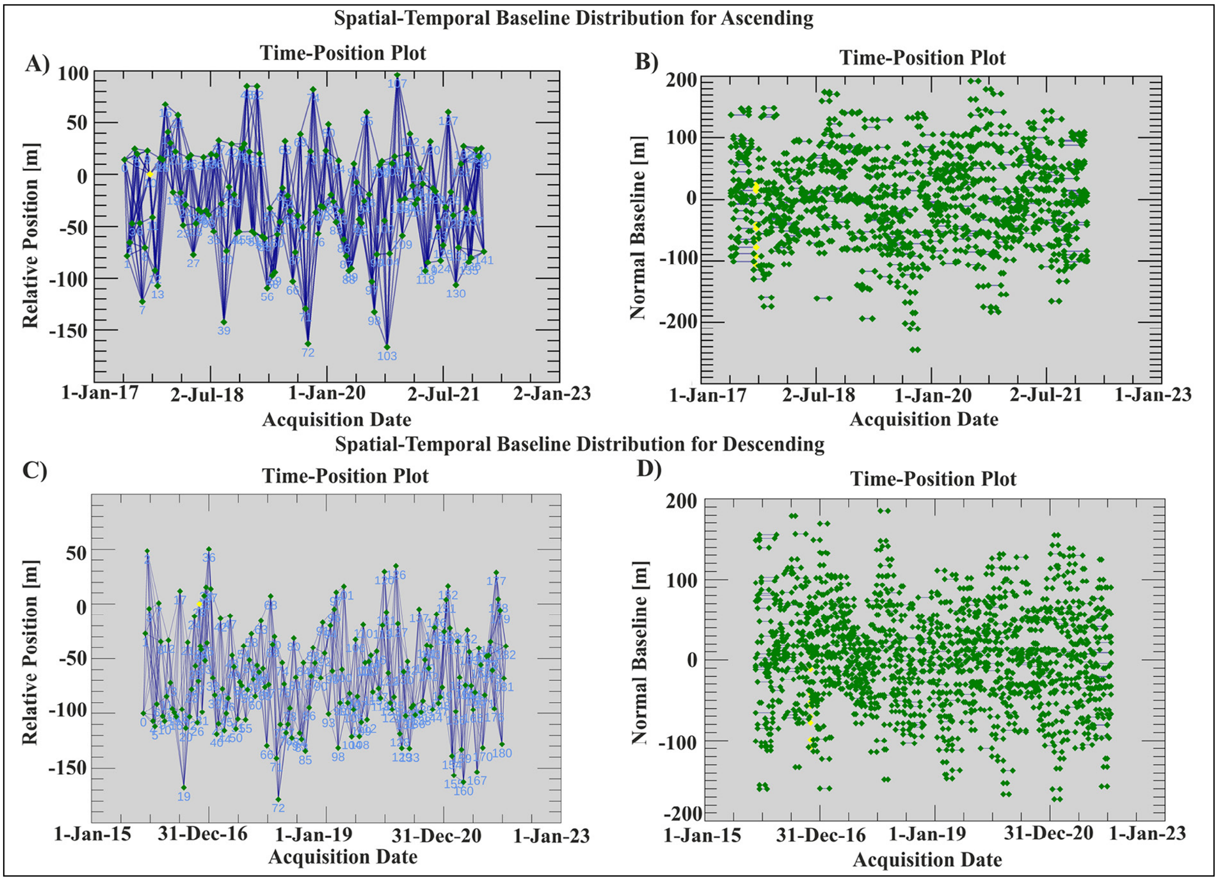

Figure 3- a) and b) Links between the pairs of SAR images showing the spatio-temporal distribution for ascending and descending, respectively. Each image is represented by a diamond with its ID number, c) and d) Represents the relative positions of all pairs of interferograms generated between Sentinel-1 datasets for ascending and descending, respectively. The yellow diamonds represent the reference image pair (master), while the green diamonds represent the slave image pairs. While, for ascending dataset, the date of master image is 2017/09/20, for descending dataset, the date of master image is 2016/12/31.

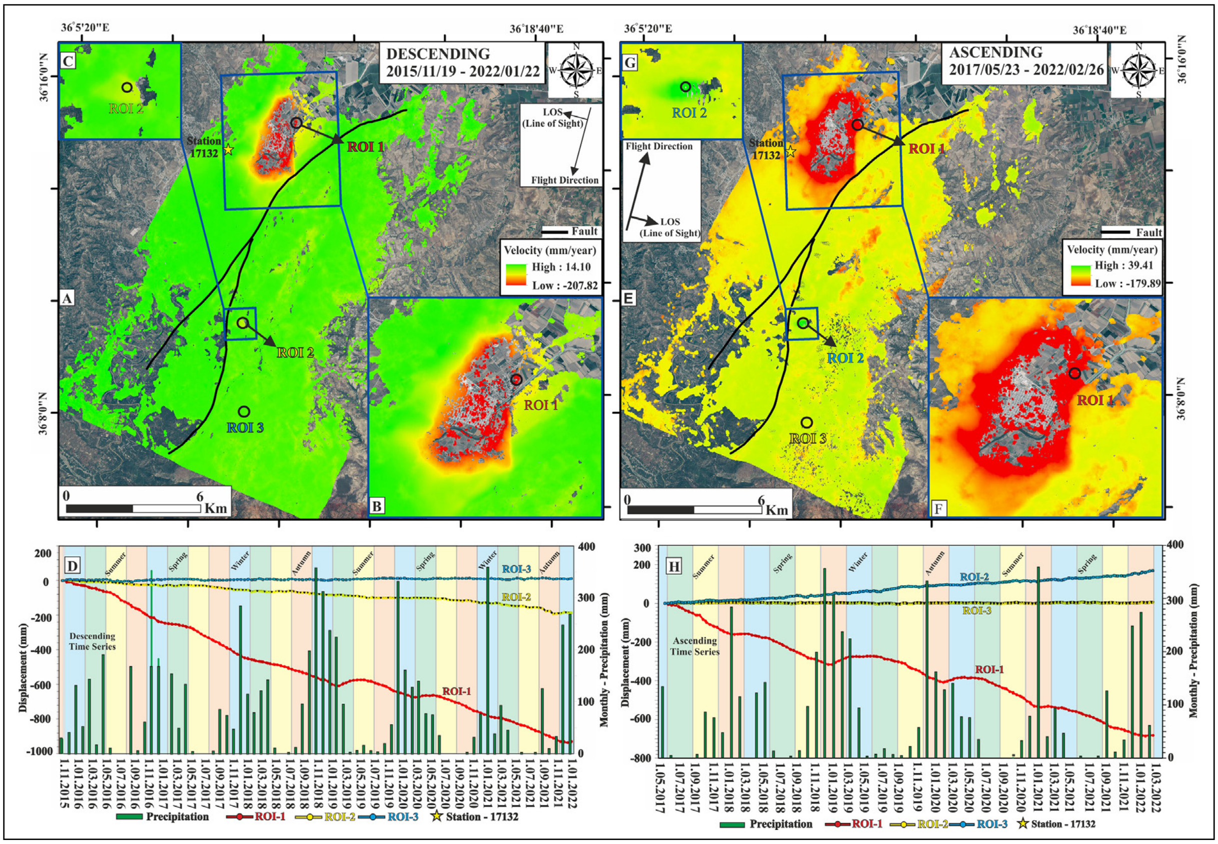

Figure 4- a) and e) Descending and ascending Sentinel-1 datasets of Hatay province illustrate the results of SBAS analysis. Positive values are interpreted as movement towards the satellite line of sight direction (LOS) and negative values as movement away from the satellite direction, b) and f) details of the industrial zone, c) and g) details of landsilde zone, d) and h) shows the time series, and bars illustrate the average monthly precipitation data provided by the General Directorate of Meteorology, and colored areas represent seasons. The black lines show the active faults published by the MTA (Emre et al., 2012).

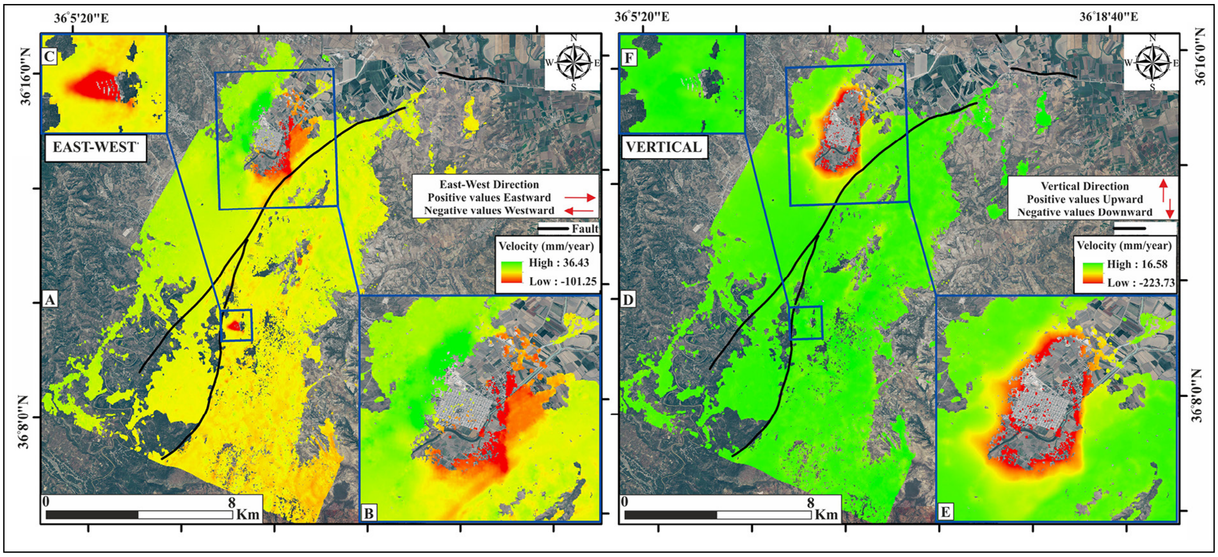

Figure 5- The result of the decomposition of Sentinel-1 descending and ascending data sets belonging to Antakya province, a) east - west component, b) details of Industrial zone, c) Landslide zone, d) vertical component, e) details of Industrial zone and f) Landslide zone. Positive values indicate uplift and negative values indicate subsidence. The black lines show the active faults published by the MTA (Emre et al., 2012).

Table 2- Max and Min velocities and displacement values from Figures 4 and 5.

	Max Velocities (cm/year)	Min Velocities (cm/year)	ROI-1 Displacement (cm)	ROI-2 Displacement (cm)	ROI-3 Displacement (cm)
Ascending 2017/05/23 - 2022/02/26	3.94 cm/year	-17.98 cm/year	~ -70 cm	~ 20 cm	~ 0 cm
Descending 2015/11/19 - 2022/01/22	1.41 cm/year	-20.78 cm/year	~ -90 cm	~ -20 cm	~ 0 cm
Vertical	1.65 cm/year	-22.37 cm/year			
East-West	3.64 cm/year	10.12 cm/year			

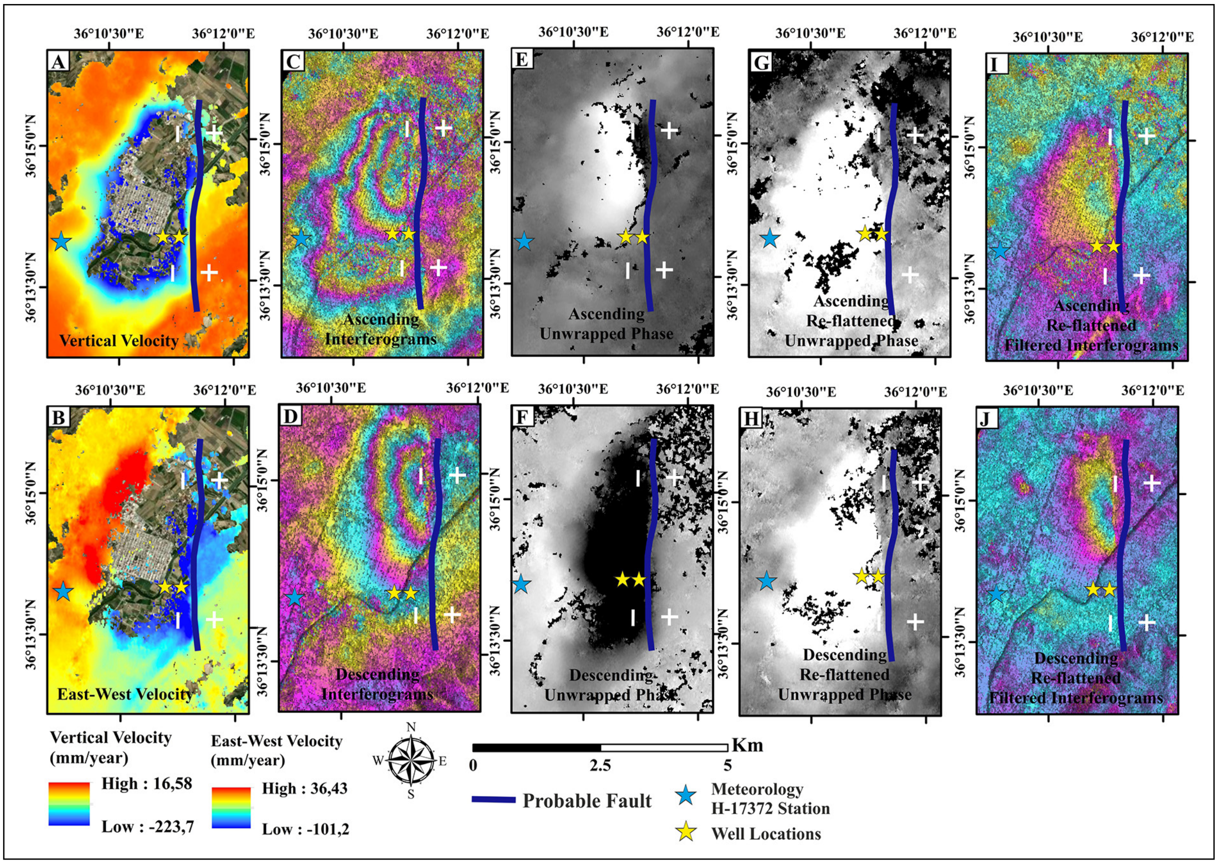

Figure 6- Deformation area of industrial zone of the Hatay province, a) Uplift - subsidence deformations. Positive values indicate an uplift; negative values indicate a subsidence, b) East-west deformations, Positive values mean east direction, and negative values mean west direction, c) and d) ascending (2018/07/29 – 2018/09/27) and descending (2019/12/28-2020/02/14) interferogram examples, e) and f) ascending and descending unwrapped phases, g) and h) ascending and descending re-flattened unwrapped phases, i) and j) ascending and descending re-flattened filtered interferograms, respectively.

which is seen in both ascending and descending data in both interferograms and unwrapped phases. Based on the well information in figures 1f and 1g and the data in Figure 6, the eastern boundary of the deformation zone indicates a probable normal fault.

In Figures 7a and 8a, the time series profiles obtained from the ascending and descending SBAS results of the Industrial zone of Hatay province and the Google Earth profiles corresponding to the relevant profiles are shown, respectively. Both figures depict the deformation amounts in the time series in the LOS direction. In Figures 7a and 8a, a sharp deformation area was determined in the area to the northwest of the industrial zone in the area where the meandering of the Asi River begins (Figure 7a - profiles B-B’, C-C’ and H-H’; and Figure 8a profiles C-C’ and H-H’). Surface deformations, which are relatively similar to the bowl structure, have been observed in the remaining regions

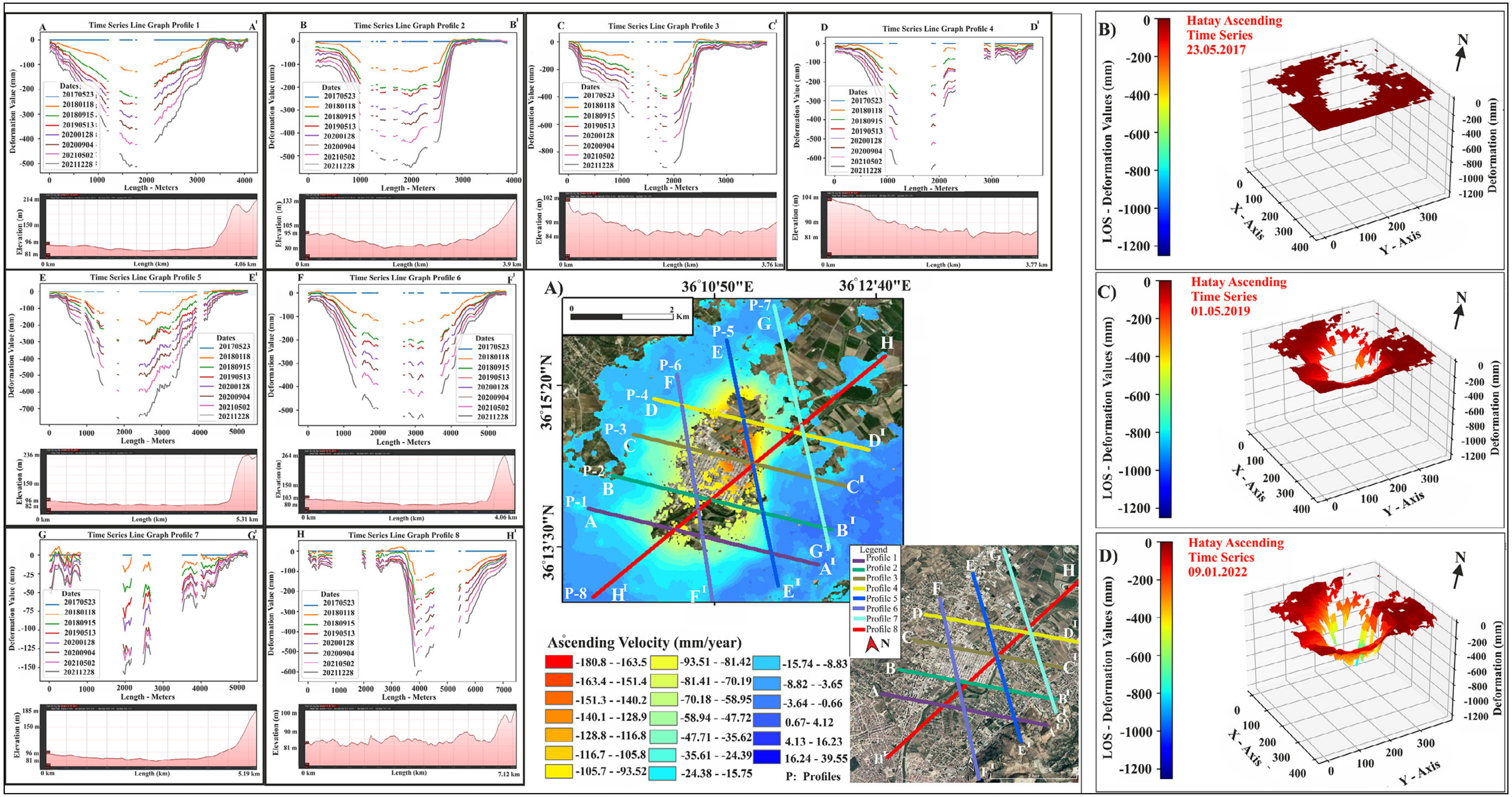

Figure 7- a) Time series cross sections for ascending geometry and google earth terrain profiles of the Hatay industrial zone, The amount of velocity in time series interprets as the direction of LOS, b), c) and d) 3D view of the time series corresponding to the specified dates for ascending geometry.

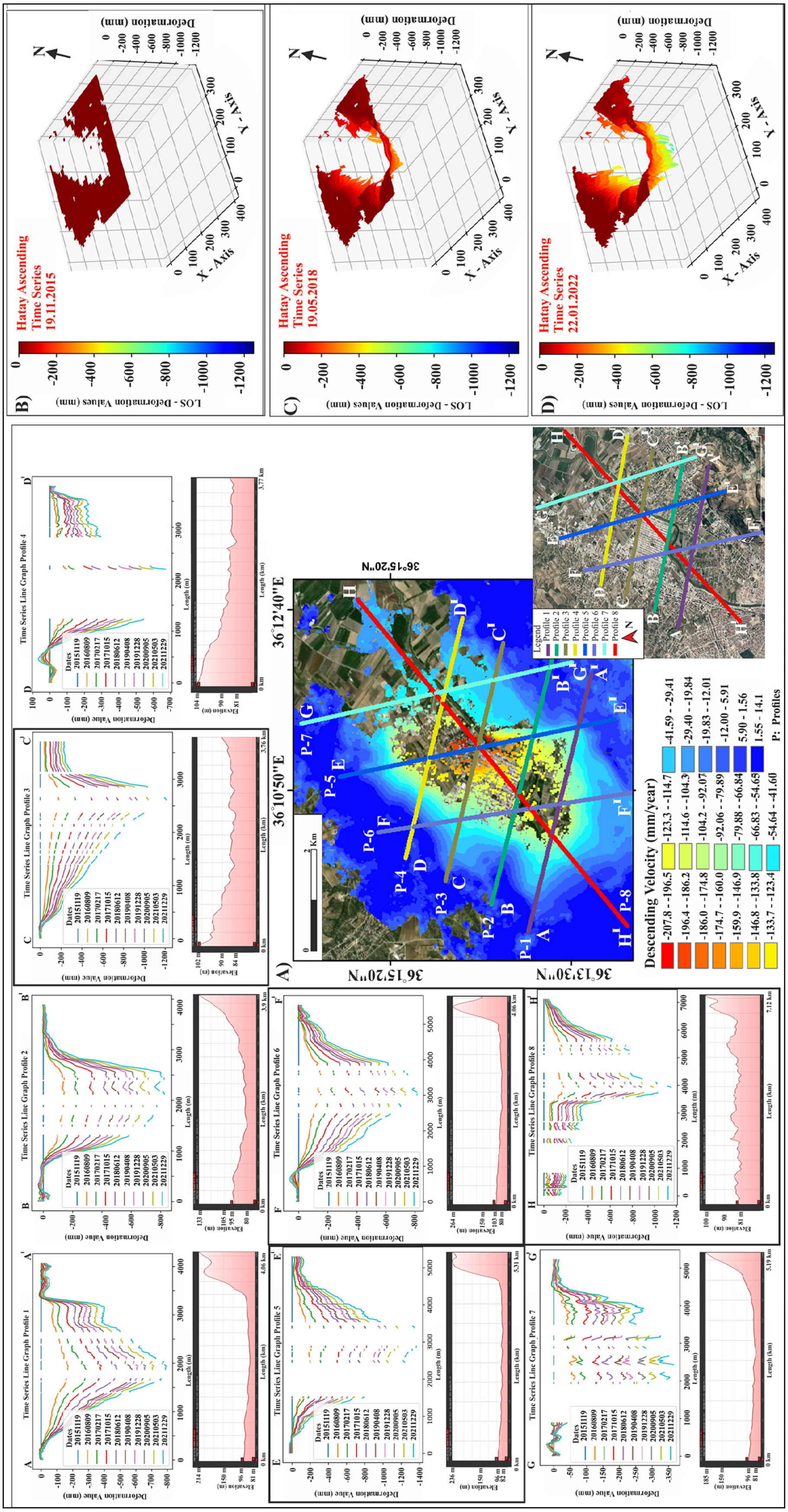

Figure 8- a) Time series cross sections for descending geometry and google earth terrain profiles of the Hatay industrial zone. The amount of velocity in time series interprets as the direction of LOS, b), c) and d) 3D view of the time series corresponding to the specified dates for descending geometry.

except for the northwest of the industrial zone (Figure 7a profiles A-A', E-E' and F-F' and; Figure 8a profiles E-E' and F-F'). Figures 7b and 8b show the 3D view of the time series corresponding to the dates for ascending and descending geometries, respectively.

The second deformation area is the landslide zone located in the central part of the study area (Figure 9). Figure 9a shows the 3D image of the landslide zone obtained from the orthophotos and Figure 9b shows the satellite orbital movements. Figure 9c shows the deformation field of the landslide zone obtained from the data with ascending geometry. Red areas show movement towards the satellite direction (LOS direction) with a velocity of 3.0 cm/year. In Figure 9d, the area of deformation with light green, there is a movement away from the satellite direction (LOS direction) at a rate of 4.5 cm/year. Figure 9e shows movements in east-west direction. There is a westward movement of the landslide zone at a rate of approximately -8.5 cm/year (Figure 9e). Figure 9f shows the vertical movements in the landslide zone. Accordingly, the landslide zone shows a subsidence at a rate of approximately 4 cm/year (Figure 9f). Figure 9g shows the east-west oriented A-A′ elevation profile taken from Google Earth.

The results obtained are divided into two parts. Accordingly, the first study area is the industrial zone and the second area is the landslide zone. In the following sections, their deformations were characterized in detail.

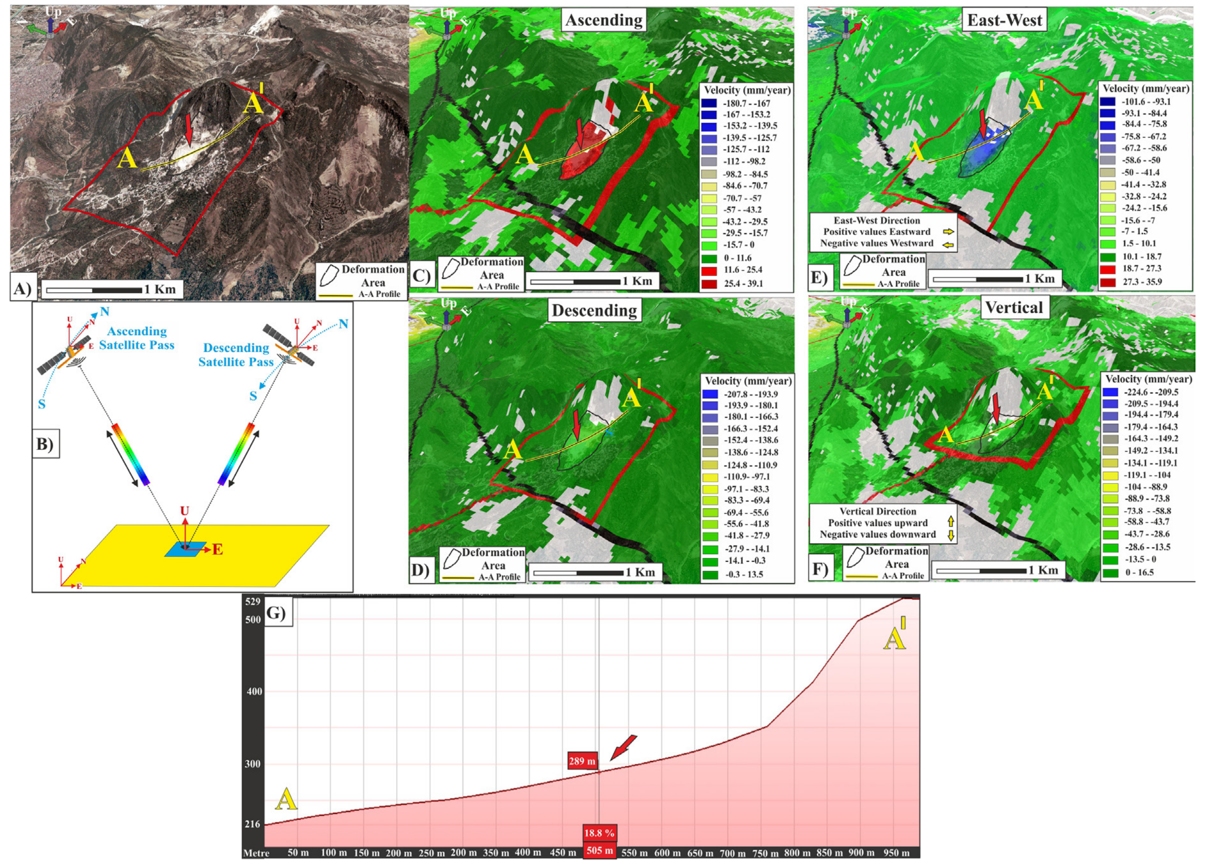

Figure 9- Deformation images of the landslide zone, a) 3D image created from orthophotos of the landslide zone, b) Satellite movement geometries, c) and d) ascending and descending velocity of deformation. While positive values are interpreted as movements towards the satellite direction, negative values are interpreted as movements away from the satellite direction, e) East - west deformations. Positive values are interpreted in the east direction and negative values are interpreted in the west direction, f) Vertical deformation. Negative values indicate subsidence and positive values indicate uplifting, g) Elevation profile from Google Earth corresponding to profile A-A′ in figures 12a, 12c, 12d and 12e.

4.2. Evaluation of Surface Deformations of the Industrial Zone

In the industrial zone located northwest of the study area, the surface deformation in both the east-west direction (Figure 5b) and subsidence (Figure 5e) is observed in an area of approximately 9.5 km². According to the profiles taken from Figures 8, 9, 10, and 11 it is evident that there is a bowl structure.

It was observed that the eastern part of this bowl structure moved relatively faster than the western part (Figure 5b). In the profiles taken from the deformation areas, obtained from the ascending and descending datasets (Figures 8 and 10) and the 3D models (Figures 13 and 15), a sharp deformation difference occurs in the eastern border of the deformation area. The deformation is caused by different geological units in the eastern and western regions and the presence of a probable fault system (Figures 1f and 1g). In Figure 1g, the well log 55260, which is close to the center of the deformation zone, shows that the clay unit reaches about 150 m in thickness. However, in Figure 1f, the well log 41982 obtained from the eastern part of the deformation zone shows that this same clay unit becomes thinner (8 m thick) and cuts sandstone and limestone. For this reason, it was determined that the deformation in the relatively less resistant clay unit reaching 150 m was higher than the more resistant sandstone and limestone in the eastern region, leading to a sharp deformation difference between these two units. For this reason, a probable fault plane between the two units was considered as shown in Figure 12A. This probable fault structure is also supported by the interferograms in Figure 6, which show that the fringe patterns become widen towards the west and are abruptly interrupted in the east (Figure 6). This probable fault zone is visible in the time series profiles (C-C’- H-H’) taken from Figures 8 and 10.

From the time series of the deformation fields obtained from ascending and descending geometries (Figures 4d and 4h), it is seen that the deformations

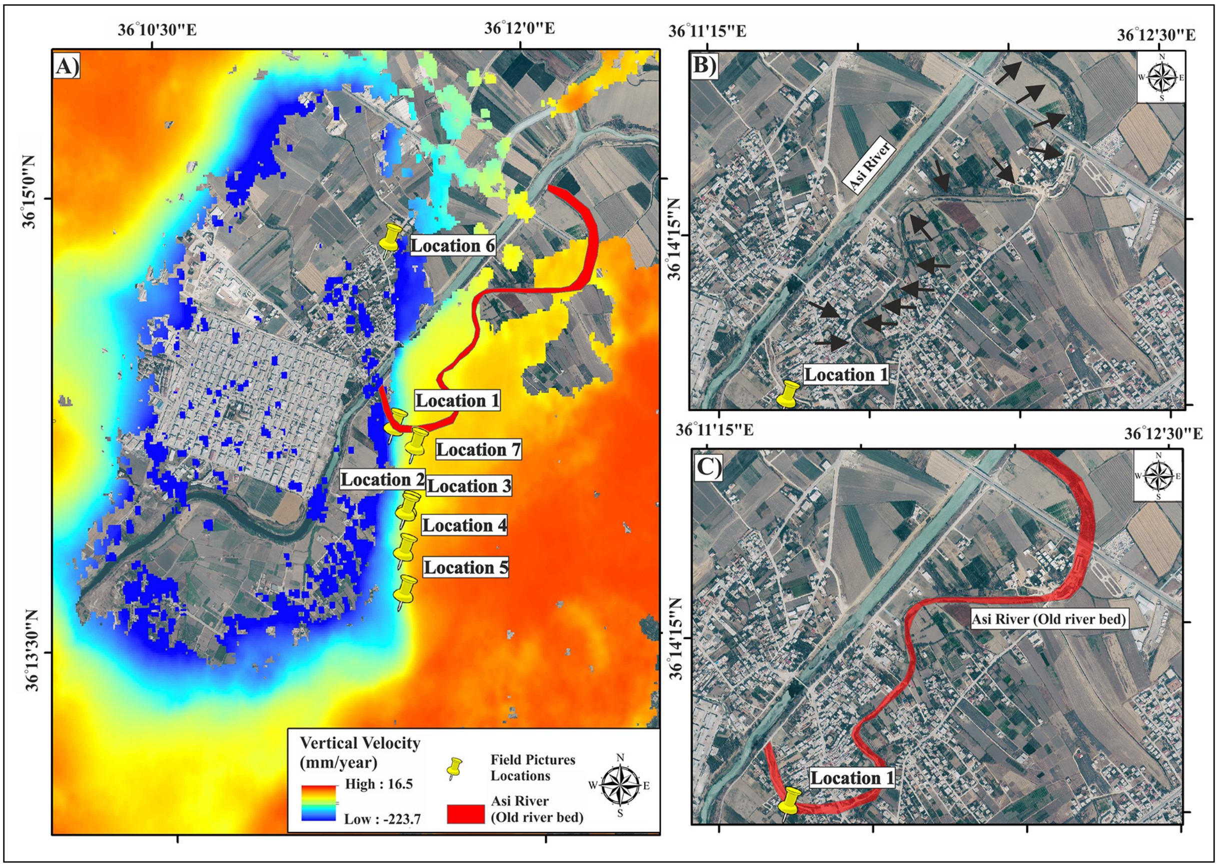

Figure 10- a) The vertical deformation for the industrial zone and the locations of the photos taken from the field (Figure 10a taken from Figure 5e). Positive values show uplift and negative values show subsidence, b) and c) old river bed detected from orthophoto images.

in winter and autumn seasons are relatively less than in spring and summer seasons. The amount of deformation accelerates in summer and spring (Figures 4d and 4h). This is thought to be due to the decrease in water use in the winter and autumn months or excessive rainfall. The graphs in Figures 4d and 4h show that the amount of water that tries to reach its previous level (recharging) is due to precipitation during the autumn and winter seasons. For all these reasons it was evaluated that there was an indirect correlation between the precipitation data obtained and the deformation rate (Figures 4d and 4h).

The surface deformation in the region is thought to have several causes. The main reason is excessive or improper groundwater usage accompanied by the industrial zone laying in the center of this deformation. It is determined that this region and its surroundings have been deformed in the east - west and vertical direction, resembling a bowl structure.

The second factor that affects this deformation is the geological structure of the units in the region. The location of the well 55260, which has a thicker clay unit that is relatively less resistant, is located further west than the well 41982 which lies closer to the center of the deformation zone (Figures 1g and 1f). Given the well log data, the eastern side of the deformation area is closer to the bedrock and the sudden deformation here is associated with the probable fault plane (Figure 12a). Figures 12c and 12d show the interferogram model with surface deformation corresponding to the probable well water withdrawal and Figures 12e and 12f show the expected interferogram models with surface deformation in case of probable faulting. The interferogram structures in Figure 6 obtained as a result of data processing coincide with the interferogram patterns in Figure 12f (Figures 12g and 12h). In addition, the time series profiles as shown in Figures 12i and 12j, the sudden downward movement of the eastern side of the bowl structure and the

Figure 11- Photos were taken during field studies (Locations are shown in Figure 10a).

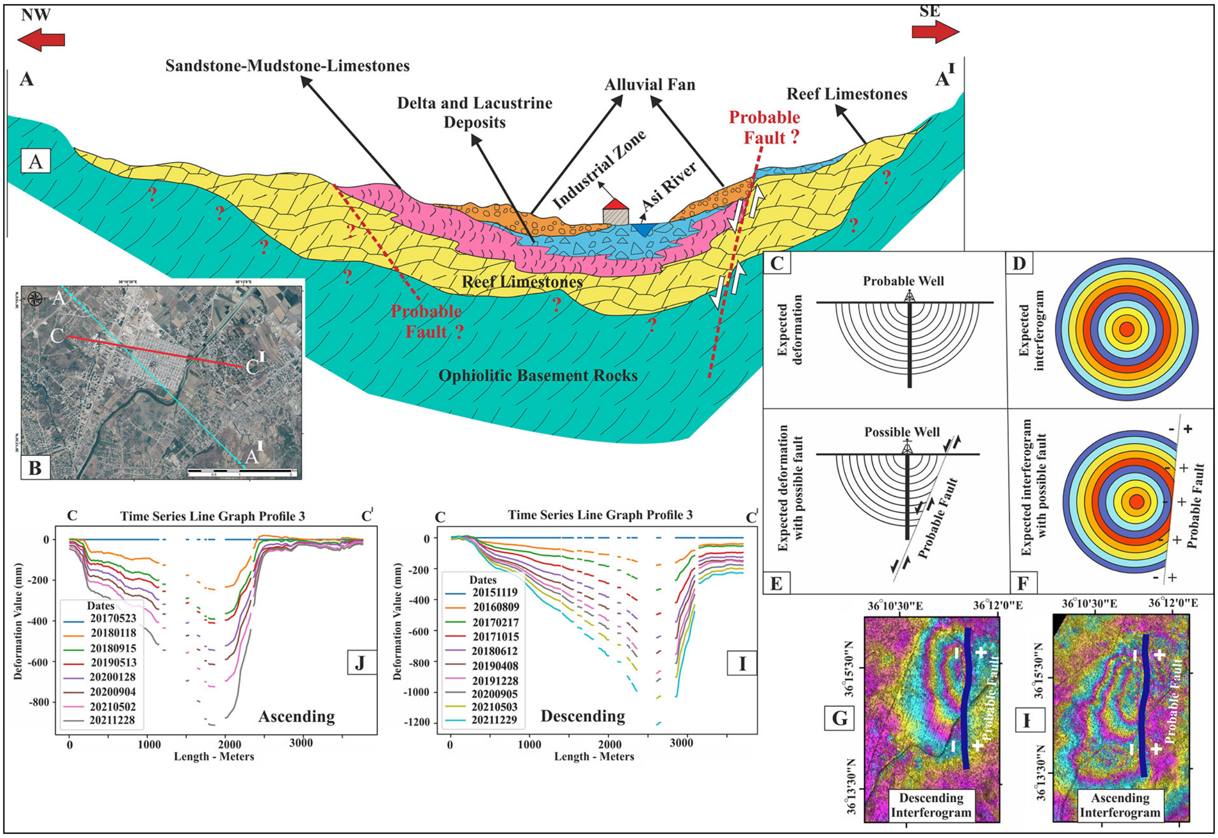

Figure 12- a) Geological cross-section and probable fault model formed on the industrial zone, b) Orthophoto image corresponding to the A-A' section, c) The expected deformation depth cross-section with possible well, d) The expected interferogram in the case of deformation due to draft in figure c, e) The expected deformation area due to the draft in the case of a probable normal fault in figure a, f) The expected interferogram in the case of deformation due to draft in Figure e, g) and h) sample interferograms were taken from Figures 6d and 6c, j) and i) time series profiles from Figures 7a and 8a.

relatively slower downward movement of the western side with certain time intervals indicate the presence of a probable fault systems on the eastern side. This occurs because the eastern block of the bowl structure is closer to the bedrock (Figure 12a).

Another factor affecting this deformation area is the meandering of the Asi River where the industrial zone is located (Figure 10a). It is considered that the velocity of the Asi River slows down in this region (due to meandering) and the amount of water accumulated here is higher than in other regions (Figure 10a). In addition, due to the reclamation of the Asi River outside the deformation area (Figures 14b and 13c), it is considered that the water velocity of the Asi River in this region has changed, its natural structure has deteriorated and this situation has affected the deformation area. The weight of the industrial zone and the use of water are foreseen as a reason also affecting the deformation in the region.

During the field surveys, it was reported that the houses and business centers in the area were affected by deformation, and even the Barış Arslan Elementary and Intermediate School (Location 5) was closed due to deformation (Figures 14h and 14i). The General Directorate of Natural Disasters Report prepared by Kuran et al. (2006), states that there was a deformation in 2004-2005 and even some houses in the region were demolished intentionally due to deformation. Viewing the results in this report in this study, it appears that the deformation in 2004 has continued until 2022.

In summary, it is thought that the main causes of deformation in the region are primarily the groundwater level and excess water use in the region due to the rainfall data, time series (Figures 4d and 4h) and the bowl-shaped structure of the deformation (Figures 8, 9, 10 and 11). Another factor is thought to be the geological structure of the region, which is located in the middle of clayey alluvial units which is compacted due to the weight of the industrial zone (Figure 1e). The proximity of the deformation area to the bedrock in the eastern parts and the thicker levels of clay units in the western parts are thought to account for the sharp deformation difference in the eastern block (Figure 12). This deformation boundary is interpreted as a probable fault due to tectonism (Figures 6 and 12). Finally, another reason affecting the deformation is the reclamation and straightening of a section of the Asi River and the meandering structure in the deformation zone (Figure 10).

Similar to the situation in Mexico City, where the surface deformation due to excessive groundwater withdrawal reached 35 cm per year (Strozzi and Wegmuller, 1999; Cabral-Cano et al., 2008; Osmanoğlu et al., 2011, Cigna and Tapete, 2021), the annual deformation in the industrial zone of the Hatay province are about 3 cm in the east direction, about 10 cm in the west direction and about 22 cm in the vertical direction.

4.3. Evaluation of the Landslide Zone Surface Deformations

The second study area where significant surface deformation is observed is the area corresponding to the landslide zone. The area of the landslide zone with a surface deformation of about 0.3 km^2 is shown in Figure 9a. The surface deformation vectors obtained in Figures 9c and 9d are decomposed into their components, as deformation movements both in the eastern direction and subsidence. It is seen that the eastward movement is about 7 cm/year and the subsidence movement is about 2 cm/year. Comparing Figures 9e and 9f, it can be seen that the velocity of the area in this region is higher for the eastern component as well as the subsidence motion. The geographical structure of the area and the eastern slope of the mountainous area support the deformation movement in the eastern direction (Figures 9a and 9g). Therefore, the deformation here is considered as a landslide zone.

5. Conclusion

It is crucial to investigate surface deformations that may occur in large cities due to the natural or anthropogenic causes and take measures for the future. In this study, the surface deformations of the Hatay province were revealed with the remote sensing method InSAR-SBAS, and the results of the study were checked by field studies, average precipitation data, well data and geological findings. Surface deformations, time series and models of the industrial and landslide zone in the study area were presented.

As a result, four main factors are thought to affect the industrial zone's deformation;

1. The most important factor affecting the deformation in the industrial zone is the groundwater level. Time series and average monthly precipitation data show that the deformation accelerates in the summer and spring, and decreases in the winter and fall. This supports the idea that the deformation in the region is related to the excess water use and precipitation rates.

2. The industrial zone is located on clayey alluvial units. Due to its weight and the geologic structure of the region, the nature of the deformation is affected. The difference in deformation rates between the eastern and western borders shows the presence of a probable fault on the eastern border. Probable fault in the study area may act as barriers to the horizontal migration of the groundwater. The fact is that the ground deformation rates are still high for most of the urban area. Improved urban planning and water management could reduce subsidence or changing water extraction from various aquifers might be the solution to prevent subsidence.

3. There is an indirect correlation between the precipitation data obtained and the deformation rate. The deformations in the winter and autumn are relatively less than in the spring and summer.

4. The meandering structure of the Asi River can affect the deformation because the changing course of the river increases the rate of deformation.

The second studied area was identified as the landslide zone which shows deformation in both eastern and vertical directions. Considering the Hatay location in the 1st degree earthquake zone, other geophysical studies are recommended for the thorough investigation of water use in the area. Further research should be conducted to determine the deformation and how could this affect the Infrastructural integrity of the city. In addition, the province of Hatay should take similar measures to that of Mexico City by prohibiting water withdrawal and drilling of new wells. Providing that the decline in water level corresponds with the decrease in subsidence in the following years.

Data Availability

Sentinel-1 data are available online through Copernicus (https://scihub.copernicus.eu) platforms. Precise orbits were downloaded from European Space Agency's Sentinel1 website (https://qc.sentinel1.eo.esa.int/, in March 2022). SRTM data are provided on Earthdata portal (https://earthdata.nasa.gov). We thank the Turkish State Hydraulic Works for providing groundwater level data and the Turkish State Meteorological Service for the precipitation data. Thanks to the European Space Agency for giving free access to the Sentinel-1 data through the Copernicus Hub.

Acknowledgments

This study was supported by the General Directorate of Mineral Research and Exploration (MTA), Department of Geological Researches, within the scope of the "Investigation of the Activity of Active Faults on Cities" Project (Project No: 2022-30-14-02-2) conducted between 2021-2022. We express our gratitude to Dr. Bahadır Şahin, Dr. Selim Özalp, Hasan Elmacı, Cem Özerk, and Adem Özata for their valuable contributions to field observations and discussions. Additionally, we thank Prof. Dr. Derman Dondurur for his constructive comments. Our thanks are also extended to Doç. Dr. Şule Gürboğa, the editor of the Bulletin of Mineral Research and Exploration, and the three referees. Finally, we convey our deepest appreciation and heartfelt gratitude to Tiffany Faller Karaca for her support.

References

Aimaiti, Y., Yamazaki, F., Liu, W., Kasimu, A. 2017. Monitoring of land-surface deformation in the Karamay oilfield, Xinjiang, China, using SAR interferometry. Applied Sciences 7, 8.

Amelung, F., Galloway, D. L., Bell, J. W., Zebker, H. A., Laczniak, R. J. 1999. Sensing the ups and downs of Las Vegas: InSAR reveals structural control of land subsidence and aquifer-system deformation. Geology 27, 6, 483–486.

Anderssohn, J., Wetzel, H. U., Walter, T. R., Motagh, M., Djamour, Y., Kaufmann, H. 2008. Land subsidence pattern controlled by old alpine basement faults in the Kashmar Valley, northeast Iran: Results from InSAR and leveling. Geophysical Journal International 174, 1, 287–294.

Aslan, G., Çakır, Z., Ergintav, S., Lasserre, C., Renard, F. 2018. Analysis of secular ground motions in istanbul from a long-term InSAR time-series (1992-2017). Remote Sensing 10, 3.

Aslan, G., Çakir, Z., Lasserre, C., Renard, F. 2019. Investigating subsidence in the Bursa Plain, Turkey, using ascending and descending sentinel-1 satellite data. Remote Sensing 11, 1.

Béjar-Pizarro, M., Guardiola-Albert, C., García-Cárdenas, R. P., Herrera, G., Barra, A., Molina, A. L., Tessitore, S., Staller, A., Ortega-Becerril, J. A., García-García, R. P. 2016. Interpolation of GPS and geological data using InSAR deformation maps: Method and application to land subsidence in the alto guadalentín aquifer (SE Spain). Remote Sensing 8, 11._

Bell, J. W., Amelung, F., Ferretti, A., Bianchi, M., Novali, F. 2008. Permanent scatterer InSAR reveals seasonal and long-term aquifer-system response to groundwater pumping and artificial recharge. Water Resources Research 44, 2.

Berardino, P., Fornaro, G., Lanari, R., Sansosti, E. 2002. A new algorithm for surface deformation monitoring based on small baseline differential SAR interferograms. IEEE Transactions on Geoscience and Remote Sensing 40,1, 2375–2383.

Brunori, C. A., Bignami, C., Albano, M., Zucca, F., Samsonov, S., Groppelli, G., Norini, G., Saroli, M., Stramondo, S. 2015. Land subsidence, ground fissures and buried faults: InSAR monitoring of Ciudad Guzmán (Jalisco, Mexico). Remote Sensing 7, 7, 8610–8630.

Burgmann, R., Rosen, P. A., Fielding, E. J. 2000. Synthetic aperture radar interferometry to measure earth's surface topography and its deformation. Annual Review of Earth and Planetary Sciences 28.

Cabral-Cano, E., Dixon, T. H., Miralles-Wilhelm, F., Díaz-Molina, O., Sánchez-Zamora, O., Carande, R. E. 2008. Space geodetic imaging of rapid ground subsidence in Mexico City. Bulletin of the Geological Society of America 120, 11–12, 1556–1566.

Cabral-Cano, E., Solano-Rojas, D., Oliver-Cabrera, T., Wdowinski, S., Chaussard, E., Salazar-Tlaczani, L., Cigna, F., DeMets, C., Pacheco-Martínez,

J. 2015. Satellite geodesy tools for ground subsidence and associated shallow faulting hazard assessment in central Mexico. Proceedings of the International Association of Hydrological Sciences 372, 255–260.

Conesa-García, C., Tomás, R., Herrera, G., López-Bermúdez, F., Cano, M., Navarro-Hervás, F., Pérez-Cutillas, P. 2016. Deformational behaviours of alluvial units detected by advanced radar interferometry in the vega media of the segura river, southeast spain. Geografiska Annaler, Series A: Physical Geography 98, 1, 15–38.

Cigna, F., Tapete, D. 2021. Present-day land subsidence rates, surface faulting hazard and risk in Mexico City with 2014–2020 Sentinel-1 IW InSAR. Remote Sensing of Environment 253.

DSİ, 2022. General Directorate of General Directorate of State Hydraulic Works.

Emre, Ö., Duman, T. Y., Olgun, Ş., 2012. 1:250,000 Scale Active Fault Map Series of Turkey, Antakya (NJ 37-13) Quadrangle. Serial Number: 39 General Directorate of Mineral Research and Exploration, Ankara, Turkey.

Ford, D., Williams, P. W. 1989. Karst Geomorphology and Hydrology. Unwin Hyman, London/Boston.

Hung, W. C., Hwang, C., Chen, Y. A., Chang, C. P., Yen, J. Y., Hooper, A., Yang, C. Y. 2011. Surface deformation from persistent scatterers SAR interferometry and fusion with leveling data: A case study over the Choushui River Alluvial Fan, Taiwan. Remote Sensing of Environment 115, 4, 957–967.

İmamoğlu, M., Kahraman, F., Cakir, Z., Sanli, F. B. 2019. Ground deformation analysis of Bolvadin (W. Turkey) by means of multi-temporal InSAR techniques and sentinel-1 data. Remote Sensing 11, 9.

Karaca, S. O., Abir, I. A., Khan, S. D., Özsayın, E., Qureshi, K. A. 2021. Neotectonics of The Western Suleiman Fold Belt, Pakistan: Evidence for bookshelf faulting. Remote Sensing 13, 18.

Khan, S. D., Huang, Z., Karacay, A. 2014. Study of ground subsidence in northwest Harris county using GPS, LiDAR, and InSAR techniques. Natural Hazards 73, 3, 1143–1173.

Khan, S. D., Gadea, O. C. A., Tello Alvarado, A., Tirmizi, O. A. 2022. Surface Deformation Analysis of the Houston Area Using Time Series Interferometry and Emerging Hot Spot Analysis. Remote Sensing 14, 15.

Kuran, U., Gürbüz, M., Mirzaoğlu, M., Şahinbaz, D., Eravcı, B., Yaman., M. 2006. Antakya-Güzelburç Belediyesi Yerleşim Sahasına Ait Jeolojik ve Jeofizik Ön Etüt Raporu, Afet İşleri Genel Müdürlüğü Deprem Araştırma Dairesi.

Liu, X., Zhao, C., Zhang, Q., Peng, J., Zhu, W., Lu, Z. 2018. Multi-temporal loss landslide inventory mapping with C-, X- and L-band SAR Datasets-A case study of Heifangtai loess landslides, China. Remote Sensing 10, 11.

Liu, X., Zhao, C., Zhang, Q., Lu, Z., Li, Z., Yang, C., Zhu, W., Liu-Zeng, J., Chen, L., Liu, C. 2021. Integration of Sentinel-1 and ALOS/PALSAR-2 SAR datasets for mapping active landslides along the Jinsha River corridor, China. Engineering Geology 284.

López-Quiroz, P., Doin, M. P., Tupin, F., Briole, P., Nicolas, J. M. 2009. Time series analysis of Mexico City subsidence constrained by radar interferometry. Journal of Applied Geophysics 69, 1, 1–15.

Mahmoud, S., Reilinger, R., McClusky, S., Vernant, P., Tealeb, A. 2005. GPS evidence for northward motion of the Sinai Block: Implications for E. Mediterranean tectonics. Earth and Planetary Science Letters 238, 1–2, 217–224.

Mahmouda, Y., Masson, F., Meghraoui, M., Cakir, Z., Alchalbi, A., Yavasoglu, H., Yönlü, O., Daoud, M., Ergintav, S., İnan, S. 2013. Kinematic study at the junction of the east anatolian fault and the dead sea fault from GPS measurements. Journal of Geodynamics 67, 30–39.

Massonnet, D., Feigl, K. L. 1998. Radar interferometry and its application to changes in the earth's surface. Reviews of Geophysics 36, 4, 441–500.

Motagh, M., Djamour, Y., Walter, T. R., Wetzel, H. U., Zschau, J., Arabi, S. 2007. Land subsidence in Mashhad Valley, northeast Iran: Results from InSAR, leveling and GPS. Geophysical Journal International 168, 2, 518–526.

Motagh, M., Shamshiri, R., Haghshenas Haghighi, M., Wetzel, H. U., Akbari, B., Nahavandchi, H., Roessner, S., Arabi, S. 2017. Quantifying groundwater exploitation induced subsidence in the Rafsanjan plain, southeastern Iran, using InSAR time-series and in situ measurements. Engineering Geology 218, 134–151.

Orhan, O. 2021. Monitoring of land subsidence due to excessive groundwater extraction using small baseline subset technique in Konya, Turkey. Environmental Monitoring and Assessment 193, 4..

Osmanoğlu, B., Dixon, T. H., Wdowinski, S., Cabral-Cano, E., Jiang, Y. 2011. Mexico City subsidence observed with persistent scatterer InSAR. International Journal of Applied Earth Observation and Geoinformation 13, 1, 1–12.

Raucoules, D., Colesanti, C., Carnec, C. 2007. Use of SAR interferometry for detecting and assessing ground subsidence. Comptes Rendus - Geoscience 339, 5, 289–302.

Rucci, A., Ferretti, A., Monti Guarnieri, A., Rocca, F. 2012. Sentinel 1 SAR interferometry applications: The outlook for sub millimeter measurements. Remote Sensing of Environment 120, 156–163.

Sarıfakıoğlu, E. 2018. Türkiye Jeoloji Haritaları Serisi 1/100.000 Ölçekli Antakya P36-P37 ve Hama R36 Paftaları, Maden Tetkik ve Arama Genel Müdürlüğü, Ankara.

Simons, M., Rosen, P. A. 2015. Interferometric Synthetic Aperture Radar Geodesy. In Treatise on Geophysics: Second Edition 3, 339-385.

Solari, L., del Soldato, M., Bianchini, S., Ciampalini, A., Ezquerro, P., Montalti, R., Raspini, F., Moretti, S. 2018. From ERS 1/2 to Sentinel-1: Subsidence Monitoring in Italy in the Last Two Decades. In Frontiers in Earth Science 6.

Sowter, A., bin Che Amat, M., Cigna, F., Marsh, S., Athab, A., Alshammari, L. 2016. Mexico City land subsidence in 2014–2015 with Sentinel-1 IW TOPS: Results using the Intermittent SBAS (ISBAS) technique. International Journal of Applied Earth Observation and Geoinformation 52, 230–242.

Strozzi, T., Wegmuller, U. 1999. Land Subsidence in Mexico City Mapped by ERS Differential SAR Interferometry.

Strozzi, T., Wegmiiller, U., Tosl, L., Bitelli, G., Spreckels, V. 2001. Land Subsidence Monitoring with Differential SAR Interferometry.

Şireci, N., Aslan, G., Çakir, Z. 2021. Long-term spatiotemporal evolution of land subsidence in Konya metropolitan area (Turkey) based on multisensor sar data. Turkish Journal of Earth Sciences 30, 5, 681–697.

Tomás, R., Romero, R., Mulas, J., Marturià, J. J., Mallorquí, J. J., Lopez-Sanchez, J. M., Herrera, G., Gutiérrez, F., González, P. J., Fernández, J., Duque, S., Concha-Dimas, A., Cocksley, G., Castañeda, C., Carrasco, D., Blanco, P. 2014. Radar interferometry techniques for the study of ground subsidence phenomena: A review of practical issues through cases in Spain. Environmental Earth Sciences 71, 1, 163–181.

Tomás, R., Li, Z. 2017. Earth observations for geohazards: Present and future challenges. In Remote Sensing 9, 3.

Waltham, A. C., Fookes, P. G. 2003. Engineering classification of karst ground conditions.

Wöppelmann, G., le Cozannet, G., de Michele, M., Raucoules, D., Cazenave, A., Garcin, M., Hanson, S., Marcos, M., Santamaría-Gõmez, A. 2013. Is land subsidence increasing the exposure to sea level rise in Alexandria, Egypt Geophysical Research Letters 40, 12, 2953–2957.

Yan, Y., Doin, M. P., López-Quiroz, P., Tupin, F., Fruneau, B., Pinel, V., Trouvé, E. 2012. Mexico City subsidence measured by InSAR time series: Joint analysis using PS and SBAS approaches. IEEE Journal of Selected Topics in Applied Earth Observations and Remote Sensing 5, 4, 1312–1326.

Yao, J., Yao, X., Liu, X. 2022. Landslide Detection and Mapping Based on SBAS-InSAR and PS-InSAR: A Case Study in Gongjue County, Tibet, China. Remote Sensing 14, 19.

Yao, X., Li, L., Zhang, Y., Zhou, Z., Liu, X. 2017. Types and characteristics of slow-moving slope geo-hazards recognized by TS-InSAR along Xianshuihe active fault in the eastern Tibet Plateau. Natural Hazards 88, 3, 1727–1740.

Zebker, H.A., Goldstein, R. M. 1986. Topographic Mapping from Interferometric Synthetic Aperture Radar Observations. Journal of Geophysical Research 91, 4993-4999.

Zhang, L., Lu, Z., Ding, X., Jung, H. S., Feng, G., Lee, C. W. 2012. Mapping ground surface deformation using temporarily coherent point SAR interferometry: Application to Los Angeles Basin. Remote Sensing of Environment 117, 429–439.

Zhu, W., Zhang, Q., Ding, X., Zhao, C., Yang, C., Qu, F., Qu, W. 2014. Landslide monitoring by combining of CR-InSAR and GPS techniques. Advances in Space Research 53, 3, 430–439.